Table of Contents

Section S1. Characterization of film thickness 2

Section S2. Terahertz emission from a Ni thin film 3

Section S3. Fitting results for different HM|Ni heterostructures 5

Section S4. Parameter determination for MC-TEM 9

Section S5. Time-shift analysis on terahertz waveforms 12

Section S6. Estimation of orbital-to-spin conversion ratios in Ta and Pt 15

Reference 16

S1. Characterization of film thickness

Prior to sample preparation, the deposition rates of W, Ta, and Pt were systematically calibrated using X-ray reflectometry. In Fig. S1, we present a typical X-ray reflectometry trace acquired during W deposition on an $Al_2O_3(0001)$ substrate over 1800 s. The intensity oscillations are associated with the film thickness via the relation $d \approx \frac{\lambda}{2\Delta\theta}$ under grazing-incidence conditions, where λ is the X-ray wavelength and $\Delta\theta$ is the angle difference between the neighboring interference peaks in Fig. S1. From Fig. S1, we extract a W-film thickness of d=28.4 nm, corresponding to a deposition rate of ~0.0158 nm/s. With this calibrated rate, we can calculate the linear velocity of the shutter during the preparation of wedge-shaped samples.

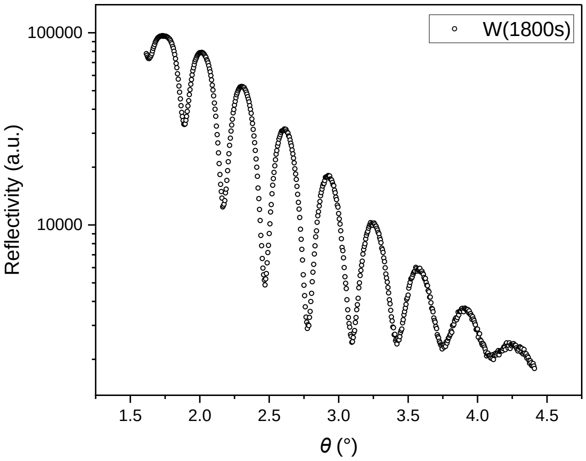

Figure S1. A typical X-ray reflectometry trace acquired during W deposition on an $Al_2O_3(0001)$ substrate over 1800 s.

After the sample preparation, the film thickness was verified *in situ* via transmission measurements using near-infrared (NIR) femtosecond laser at a wavelength of 1030 nm (Fig. S2a). In Fig. S2(b-d), we present the transmittance as a function of lateral position x for W|Ni, Ta|Ni, and Pt|Ni, each with a varying HM-layer thickness. The experimental transmittance $T = I_t/I_0$ was fitted using the transfer matrix method (TMM), treating the complex refractive indices (n+iκ) of Ni and the HM layers as fitting parameters, while assuming the nominal HM thickness gradient to be accurate. The extracted refractive indices are in general agreement with reference values[1–3], confirming the precision of our thickness control. The refractive indices obtained through fitting are provided in Table S1.

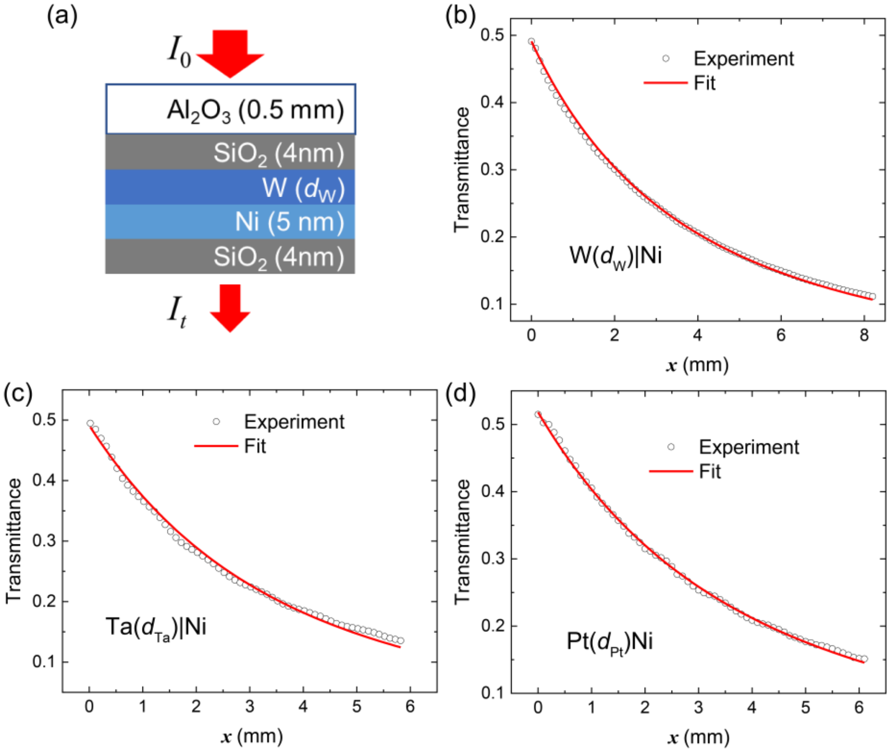

Figure S2. (a) Illustration of the transmission geometry of NIR laser through samples. **(b-c)** Transmittance results measured across the wedge-shaped samples of W(d_W)|Ni, Ta(d_{Ta})|Ni, and Pt(d_{Pt})|Ni.

Table S1. Complex refractive indices extracted from NIR transmittance measurements.

	n (experiment)	κ (experiment)
Ni	2.35	5.70
W	2.00	5.21
Ta	2.09	5.26
Pt	3.11	6.50

S2. Terahertz emission from a Ni thin film

The terahertz waveform arising from the combined the anomalous Hall effect (AHE) and magnetic dipole emission (MDE) contributions is directly extracted from the measurements on a SiO_2(4)|Ni(5)|SiO_2(4) heterostructure. The heterostructure is deposited on a 0.5-mm-thick Al_2O_3(0001) substrate, following the procedure described in Methods. The sample is excited from the substrate side, and the emitted terahertz wave is detected from the capping-layer side. The measured waveform is normalized to its peak amplitude (Fig. S3a), and denoted as the waveform $\mathcal{E}_{\mathrm{Ni}}(t)$ in the multi-component terahertz-emission model (MC-TEM).

To distinguish the contributions from AHE and MDE from the Ni thin film, we excite the SiO_2(4)|Ni(5)|SiO_2(4) heterostructure using femtosecond laser pulses from (1) the substrate side and (2) the capping-layer side. The corresponding terahertz signals, $E_{(1)}$ and $E_{(2)}$, are shown in Fig. S3b. To account for differences in terahertz and near-infrared (NIR) refractive indices between the two sides, an additional 0.5-mm-thick Al_2O_3 plate is attached to the capping-layer side[4]. The AHE and MDE components are then obtained by symmetric and antisymmetric combinations of the two waveforms: $E_{\mathrm{AHE}} = \frac{E_{(1)}-E_{(2)}}{2}$, and $E_{\mathrm{MDE}} = \frac{E_{(1)}+E_{(2)}}{2}$, as shown in Fig. 3d. Our results indicate that, in the 5-nm-thick Ni layer, the AHE and MDE contributions generate comparable terahertz radiation amplitudes.

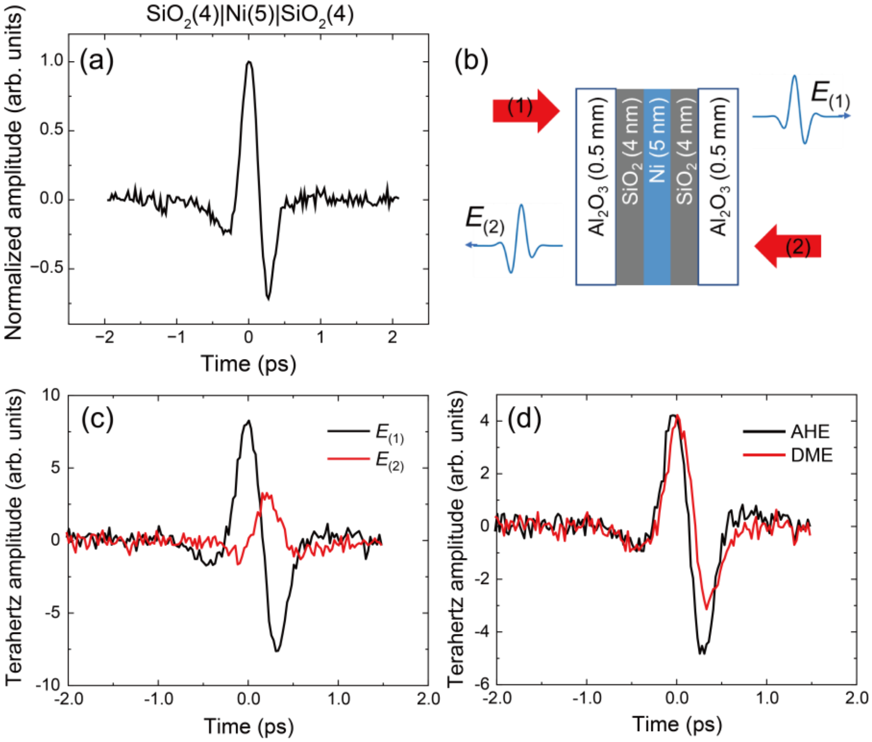

Figure S3. (a) Terahertz waveform measured from the SiO_2(4)|Ni(5)|SiO_2(4) sample. (b) Illustration of the geometry for NIR transmission measurements. (c) Terahertz waveforms obtained by exciting the heterostructure from (1) $E_{(1)}$, the substrate side and (2) $E_{(2)}$, the capping-layer side. (d) Terahertz waveforms for the AHE and MDE contributions.

S3. Fitting results for different HM|Ni heterostructures

In Fig. S4, we present the complete fitting results for the W|Ni heterostructure with different W-layer thickness d_W. The extracted terahertz waveforms from different contributions are shown in Fig. S5.

In Fig. S6, we present the complete fitting results for the Ta|Ni heterostructure with different Ta-layer thickness d_Ta. In Fig. S7a, we present the fitting results to the terahertz intensities of Ta(d_Ta)|Ni obtained via spectral integration. Figure S7b shows the absolute values of the extracted S, L and AHE+MDE contributions (A_S, A_L and $A_\mathrm{AHE+MDE}$) in Ta|Ni as functions of d_Ta. The extracted terahertz waveforms from different contributions are shown in Fig. S7c.

In Fig. S8, we present the complete fitting results for the Pt|Ni heterostructure with different Pt-layer thickness d_Pt. In Fig. S9a, we present the fitting results to the terahertz intensities of Pt(d_Pt)|Ni. Figure S9b shows the absolute values of the extracted S, L and AHE+MDE contributions (A_S, A_L and $A_\mathrm{AHE+MDE}$) in Pt|Ni as functions of d_Pt. The extracted terahertz waveforms from different contributions are shown in Fig. S9c.

The fitting program and fitting results are provided in Supplementary Data 1.

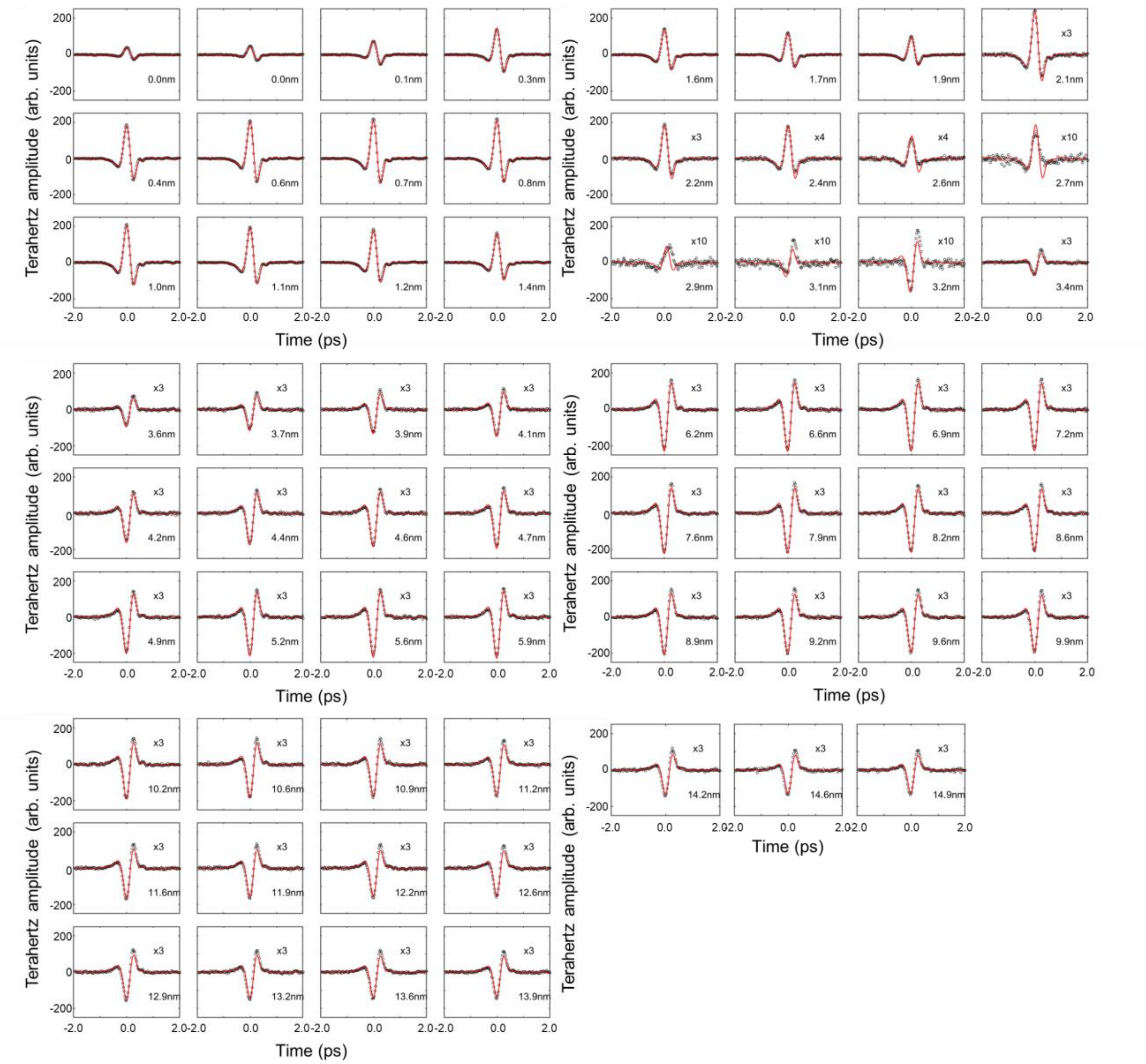

Figure S4. Fitting results to terahertz waveforms from W(d_W)|Ni heterostructures.

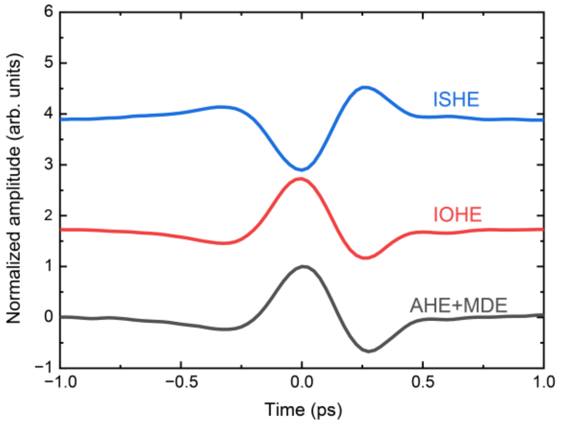

Figure S5. Extracted terahertz waveforms from ISHE, IOHE and AHE+MDE contributions in W(d_W)|Ni heterostructures.

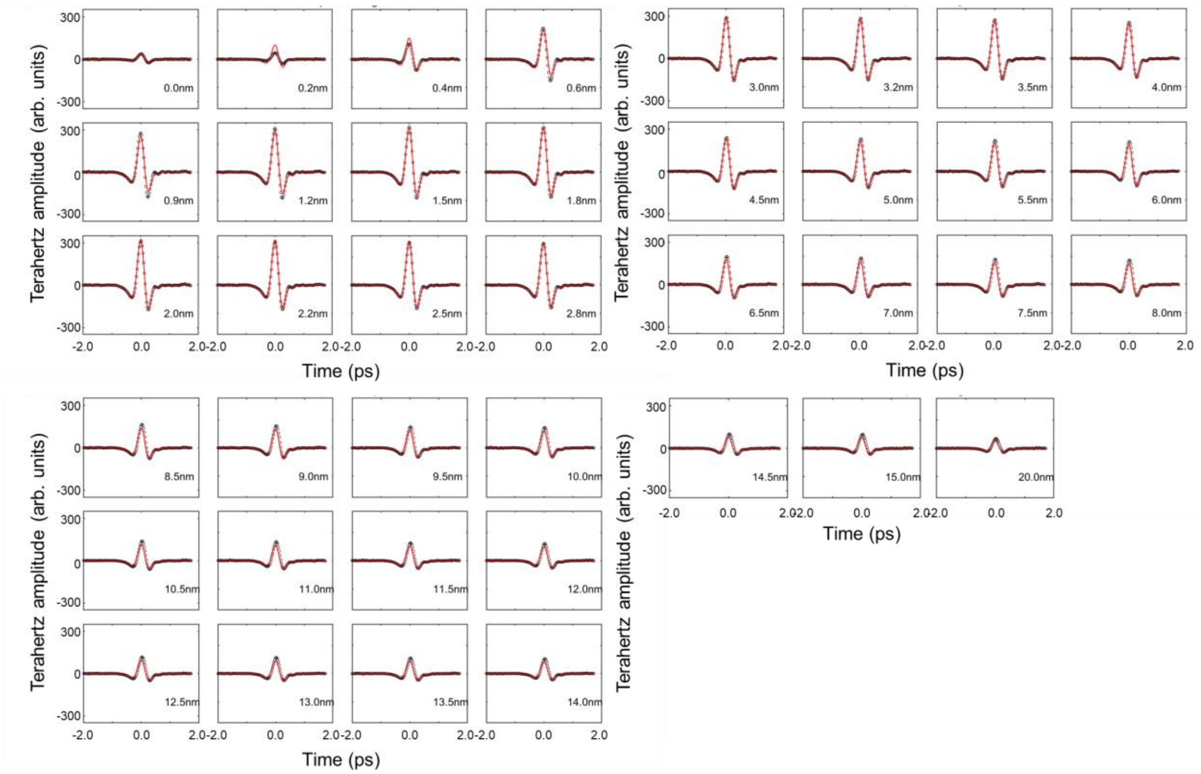

Figure S6. Fitting results to terahertz waveforms from Ta(d_{Ta})|Ni heterostructures.

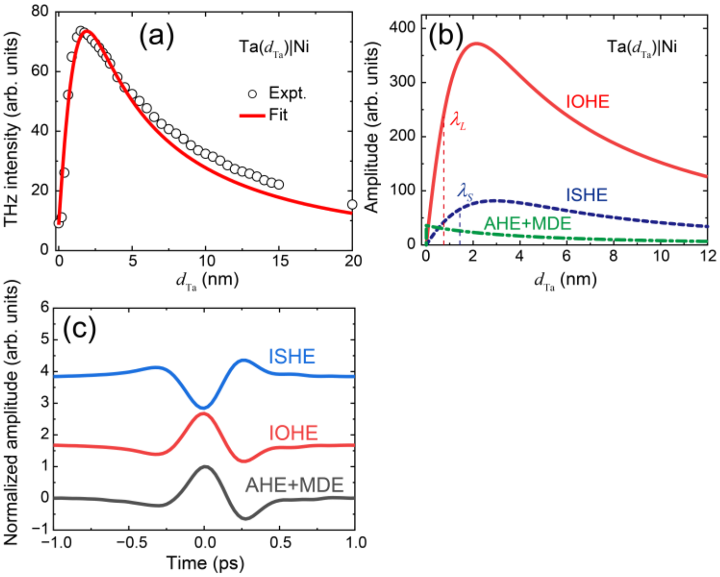

Figure S7. (a) Fitting of terahertz intensity (spectrally integrated) from Ta(d_{Ta})|Ni as a function of d_{Ta}. Symbols represent experimental data, and lines indicate model fits. **(b)** Extracted absolute amplitudes associated with the IOHE, ISHE and AHE+MDE contributions as a function of d_{Ta}. The orbital and spin MFPs are labeled. **(c)** Extracted terahertz waveforms from ISHE, IOHE and AHE+MDE contributions in Ta(d_{Ta})|Ni heterostructures.

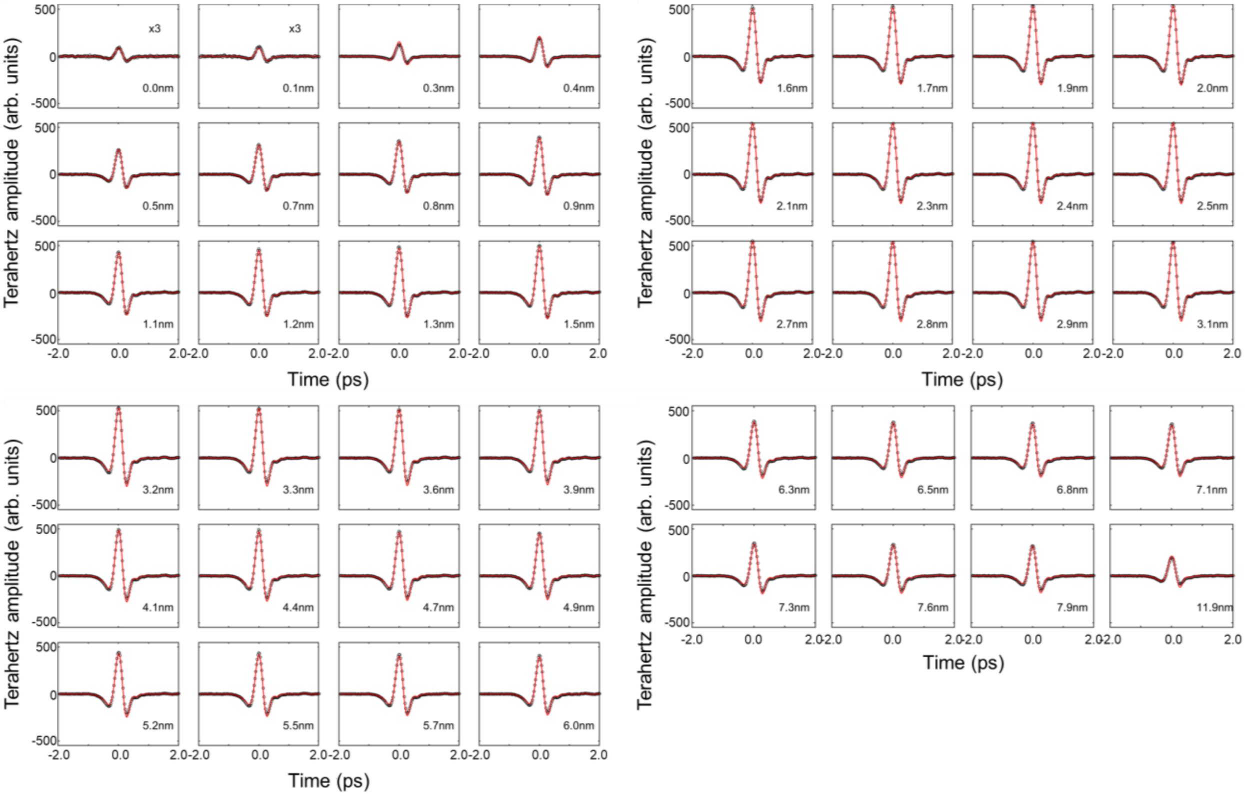

Figure S8. Fitting results to terahertz waveforms from Pt(d_{Pt})|Ni heterostructures.

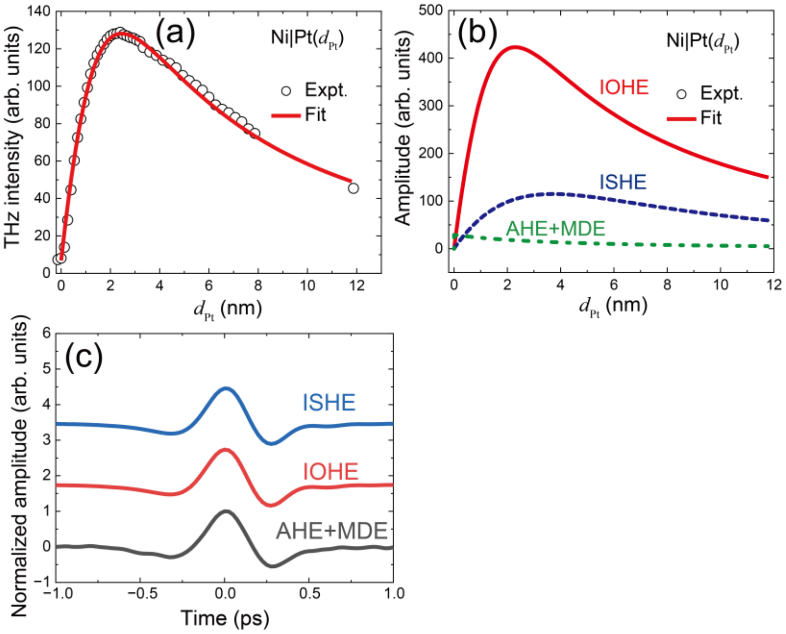

Figure S9. (a) Fitting of terahertz intensity (spectrally integrated) from Pt(d_{Pt})|Ni as a function of d_{Pt}. Symbols represent experimental data, and lines indicate model fits. **(b)** Extracted absolute amplitudes associated with the IOHE, ISHE and AHE+MDE contributions as a function of d_{Pt}. The orbital and spin MFPs are labeled. **(c)** Extracted terahertz waveforms from ISHE, IOHE and AHE+MDE contributions in Ta(d_{Pt})|Ni heterostructures.

S4. Parameter determination for MC-TEM

The substrate refractive index n_1 and the terahertz conductivities σ of metal films are experimentally determined using terahertz transmission spectroscopy. In the measurement, the terahertz transmission through free space is first recorded as a reference signal (E_{Ref}), followed by the signal transmitted through the sample (E_{Sample}). Multiple internal reflections at the interfaces are accounted for in the extraction of refractive indices (Fig. S10a). The complex transfer function is given by

$$T=\frac{E_{\mathrm{Sample}}}{E_{\mathrm{Ref}}}=\frac{2n_{(2)}\cdot\left(n_{(1)}+n_{(3)}\right)\cdot\exp\left(jk_0\left(n_{(2)}-n_{(3)}\right)d_2\right)}{\left(n_{(2)}+n_{(3)}\right)\left(n_{(1)}+n_{(2)}\right)}\cdot\frac{1}{1-\frac{n_{(2)}-n_{(3)}}{n_{(2)}+n_{(3)}}\cdot\frac{n_{(2)}-n_{(1)}}{n_{(2)}+n_{(1)}}\cdot\exp\left(2jk_0n_{(2)}d_2\right)},\qquad\text{(S1)}$$

where $n_{(1)}$, $n_{(2)}$ and $n_{(3)}$ are the refractive indices of different regions, as shown in Fig. S10a, and d is the sample thickness.

We first extract the terahertz refractive index of the 0.5-mm Al_2O_3 substrate (n_1), by setting $n_{(1)}= n_{(3)}=1.0$ (air) and $n_{(2)}= n_1$. The measured reference and sample waveforms are shown in Fig. S10b, where amplitude reduction, time delay, and waveform distortion can be observed. The corresponding amplitude and phase of the transfer function T are shown in Fig. S10c. Following the method in Ref. 5, the real and imaginary parts of n_1 are extracted (Fig. S10d), yielding a refractive index of $n_1 \approx 3.1$ in the terahertz range, consistent with previous work[6].

Next, we determine the conductivities of 5-nm-thick Ni and Fe films. For these measurements, we set $n_{(1)}=n_1 \approx 3.1$ (Al_2O_3) and $n_{(3)}=1.0$ (air). The refractive index of the metal layer is related to conductivity via $n_{(2)} \approx (1+j)\sqrt{\frac{\sigma}{2\omega\varepsilon_0}}$ at the terahertz frequencies[7], where ε_0 is the vacuum permittivity. Given that the change in phase and the absorption in the metal thin film is negligibly small: $\mathrm{Re}\left(n_{(2)}\right)k_0 d \ll 1$ and $\mathrm{Im}\left(n_{(2)}\right)k_0 d \ll 1$, the transfer function (T) simplifies to[8]

$$T = \frac{1+n_{(1)}}{1+n_{(1)}+Z_0\sigma d}\,. \tag{S2}$$

Measurements of T for Ni(5) and Fe(5) films are shown in Figs. S11a and c, and the extracted complex conductivities σ_{Ni} and σ_{Fe} are presented in Figs. S11b and d. For modeling purposes, we use the conductivities at 1.3 THz, which yields $\sigma_{\mathrm{Ni}} \approx 2.2 \times 10^6$ S/m and $\sigma_{\mathrm{Fe}} \approx 5.7 \times 10^5$ S/m.

With σ_{Ni} and σ_{Fe} determined, we further measure terahertz transmission through W|Fe(5), Ta|Fe(5), and Pt|Fe(5) samples to extract the conductivities σ_{W}, σ_{Ta}, and σ_{Pt}, as shown in Figs. S12a-c.

Finally, the amplitude coefficient b in Eq. (3) is determined by the fitting to terahertz waves generated from HM(d_{HM})|Ni when $d_{\mathrm{HM}}=0$.

A summary of the MC-TEM model parameters is provided in Table S2.

Table S2. Model parameters for the MC-TEM.

	Ni	Fe	W	Ta	Pt	Al_2O_3
σ_{FM} ($\times 10^6$ S/m)	2.2	0.57	-	-		
σ_{HM} ($\times 10^6$ S/m)	-	-	1.2	1.1	1.3	
n	-	-	-	-	-	3.1
λ_S (nm)	-	-	2.20±0.13	1.34±0.07	2.00±0.34	-
b (arb. units)	-	-	321.63	313.39	272.15	-

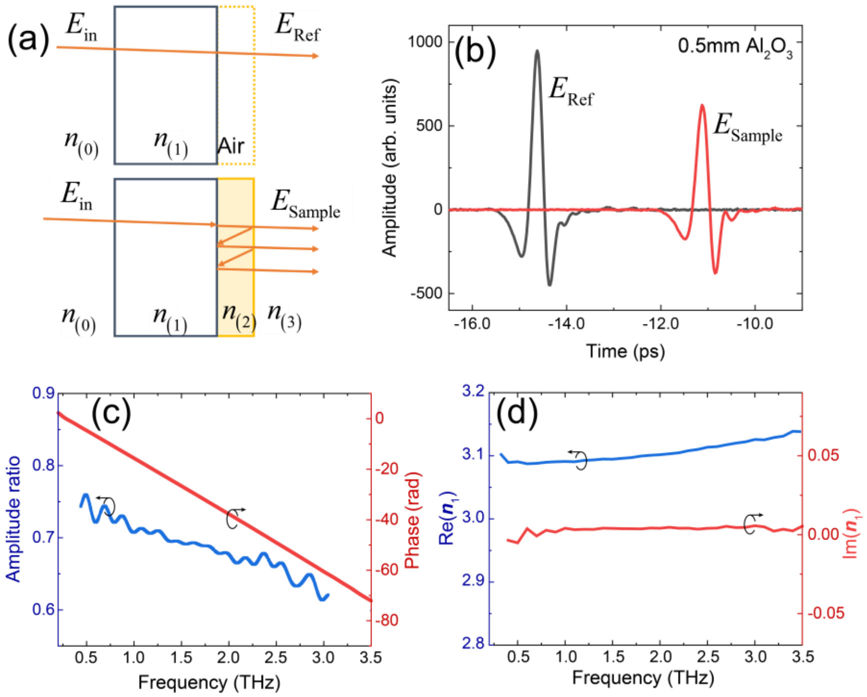

Figure S10. (a) Illustration of the geometry for terahertz transmission spectroscopy measurements. **(b)** Terahertz waveforms measured for the reference, E_{Ref}, and with sample film installed, E_{Sample}. **(c)** Amplitude and phase of the transfer function derived from the traces in **(b)**. **(d)** Real and imaginary parts of the substrate refractive index n1 obtained from **(c)**.

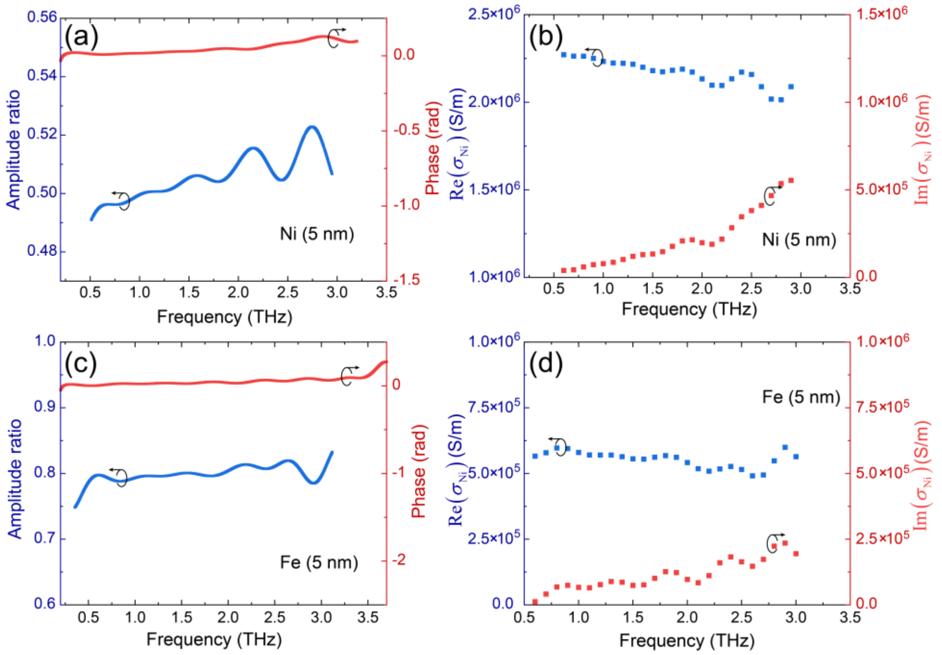

Figure S11. (a-b) Transfer function obtained from a 5-nm Ni film and the complex conductivity derived. **(c-d)** Same as **(a-b)**, but for Fe(5).

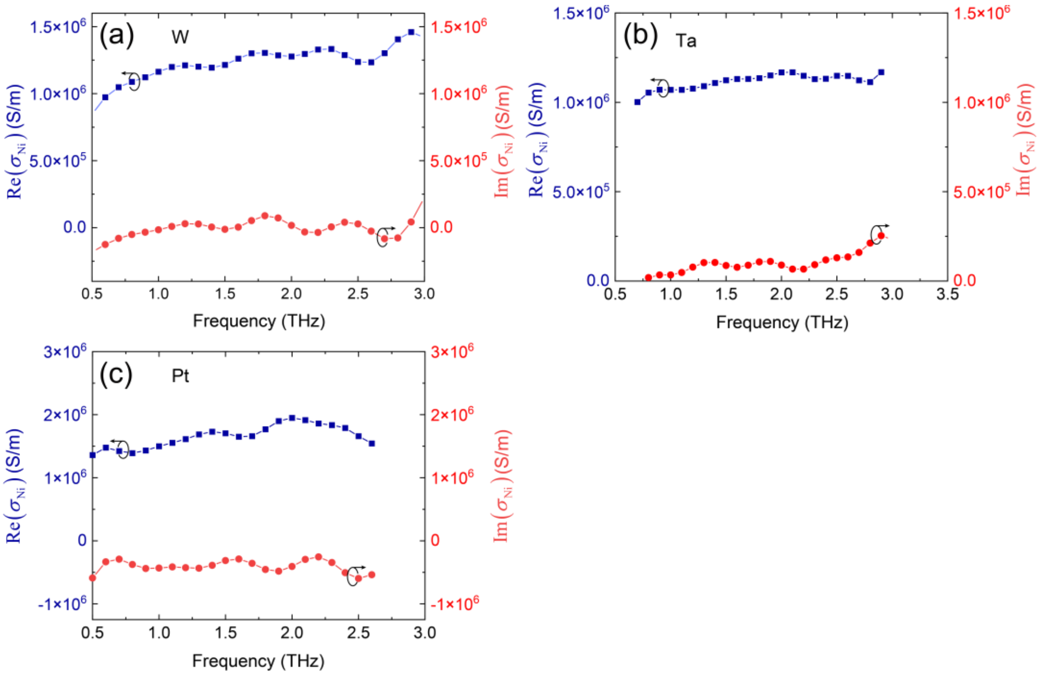

Figure S12. (a-c) Terahertz conductivities of W, Ta and Pt thin films.

S5. Time-shift analysis on terahertz waveforms

The relative time shifts of the terahertz waveforms in Fig. 4d of the main text were extracted using a fitting procedure that minimizes the mean squared error between the terahertz waveform from each SiO_2|W(d_W)|Ni sample and the reference waveform from the SiO_2|W(3.2)|Ni sample. The experimental uncertainty in the extracted time shifts was evaluated by continuously measuring the terahertz waveform from a Pt|Fe reference sample over a 14-hour period, which yielded a temporal uncertainty of approximately ±10 fs.

Notably, we do observe substantial time shifts – up to ~250 fs – in the terahertz waveforms from W(d_W)|Ni heterostructures when d_W lies between 2.0 and 3.5 nm (Fig. S13a). In contrast, for d_W>4 nm, the peak position remains essentially constant (Fig.S13b). To further confirm this behavior, we studied Ni|W(d_W) heterostructures, where the stacking order of the layers was reversed during the sample growth. As expected, the polarity of the terahertz signal is inverted (Fig. S14a). Consistent with W(d_W)|Ni, we also observe that the terahertz peak shifts up to ~175 fs for d_W=2.0 – 3.5 nm, negligible shifts occur for d_W>4 nm (Fig. S14b).

In Fig. S15, we plot the spectral intensity as a function of d_W for both W(d_W)|Ni and Ni|W(d_W) samples. Both configurations show a pronounced dip in intensity within the 2.0 – 3.5 nm range, indicating destructive interference between spin and orbital contributions. We attribute the large observed time shifts in this thickness range to such interference effects between the two components.

For comparison, Figs. S16 and S17 present the terahertz waveform variations as a function of HM-layer thickness for Ta(d_{Ta})|Ni and Pt(d_{Pt})|Ni. In these samples, where spin and orbital contributions do not interference destructively, the terahertz waveforms exhibit negligible time shifts across the wide range of HM thicknesses.

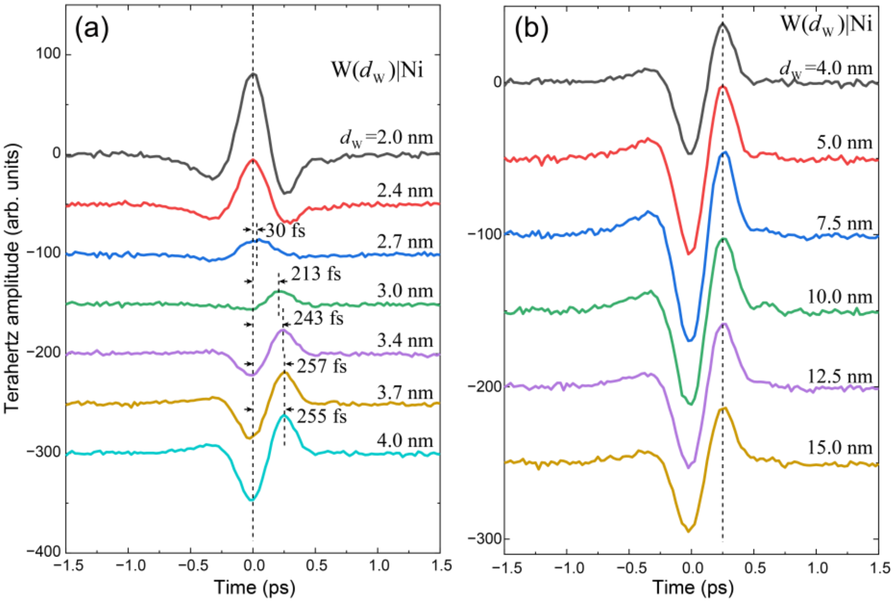

Figure S13. (a) Terahertz waveforms of W(d_W)|Ni with for d_W =2.0 – 4.0 nm. Shifts of terahertz peaks are denoted. **(b)** Same as **(a)**, but for d_W =4.0 – 15.0 nm.

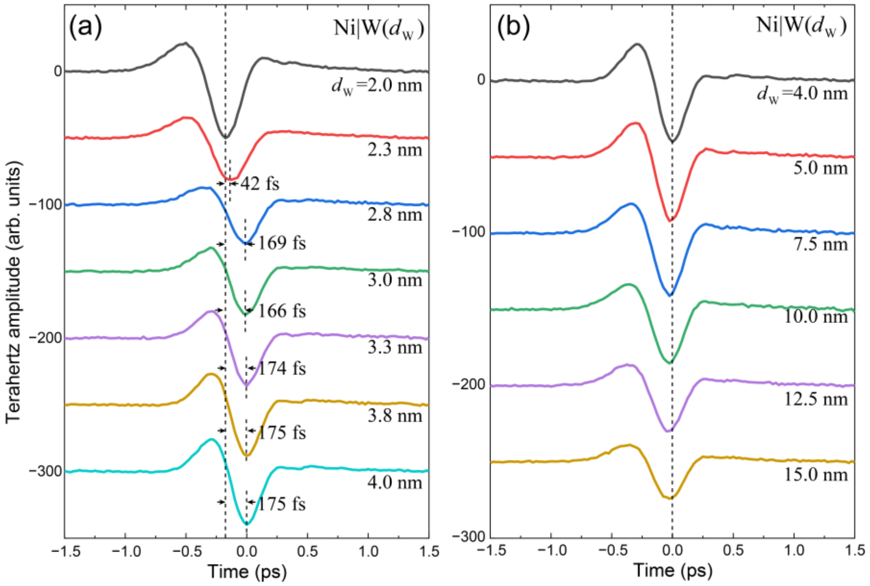

Figure S14. (a) Terahertz waveforms of Ni|W(d_W) with for d_W =2.0 – 4.0 nm. Shifts of terahertz peaks are denoted. **(b)** Same as **(a)**, but for d_W =4.0 – 15.0 nm.

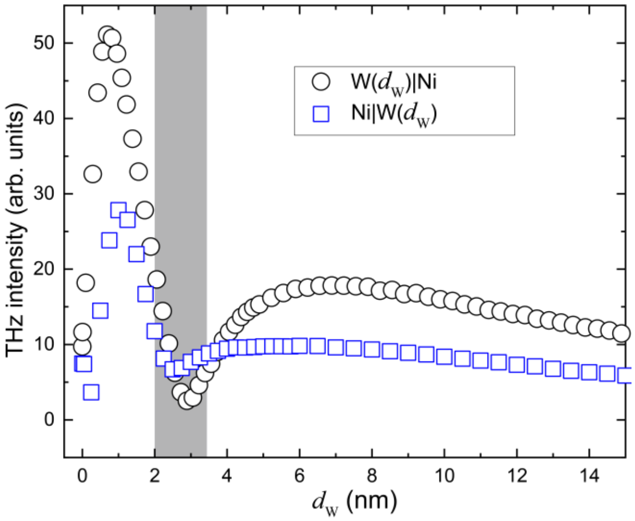

Figure S15. Spectral intensity obtained from W(d_W)|Ni and Ni|W(d_W) as functions of d_W. The thickness regime for the destructive interference between the spin and orbital signals is highlighted.

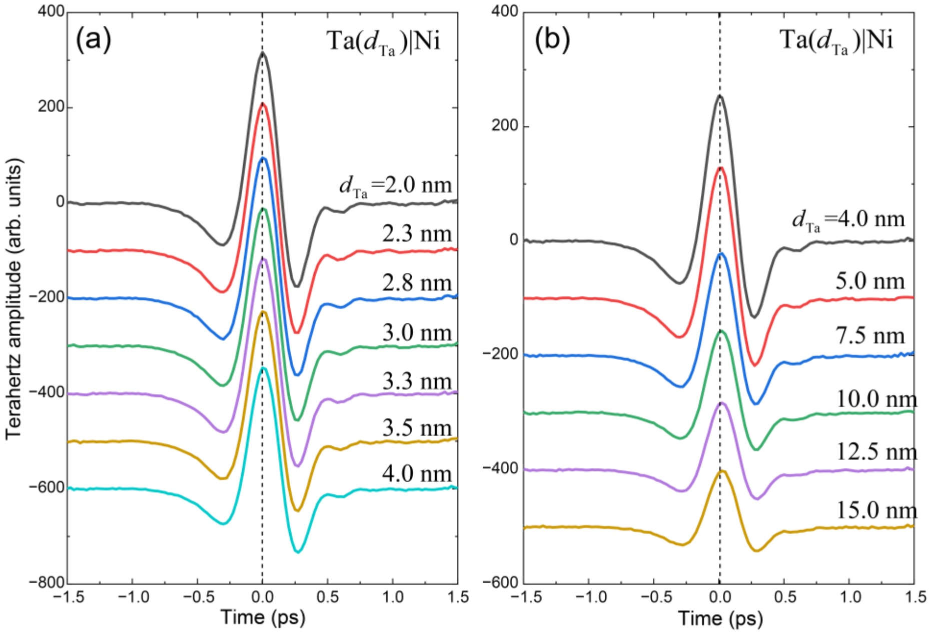

Figure S16. (a) Terahertz waveforms of Ta(d_{Ta})|Ni with for d_{Ta} =2.0 – 4.0 nm. **(b)** Same as **(a)**, but for d_{Ta} =4.0 – 15.0 nm.

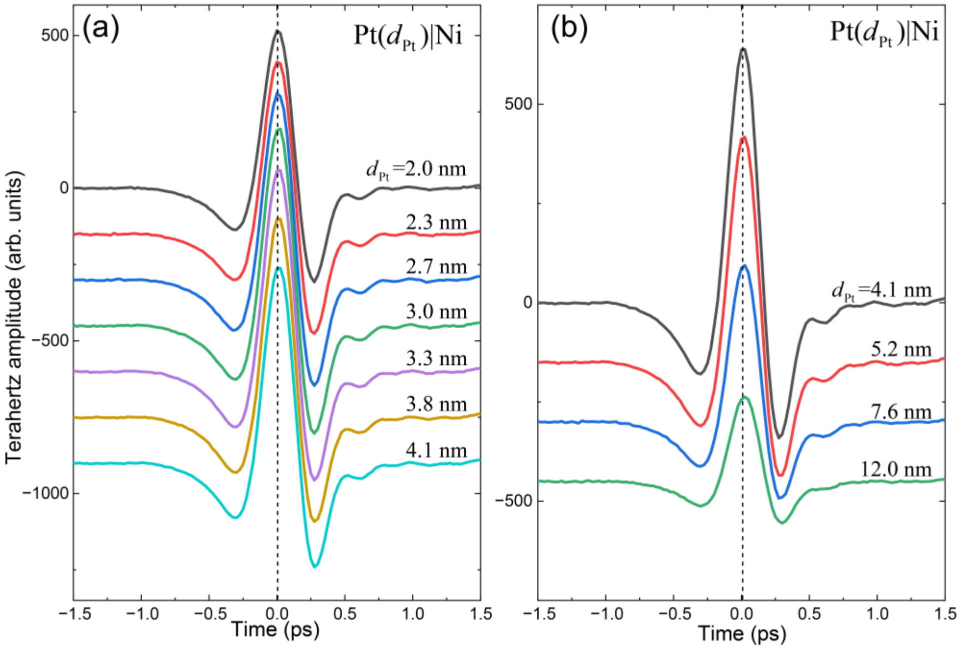

Figure S17. (a) Terahertz waveforms of Pt(d_{Pt})|Ni with for d_{Pt} =2.0 – 4.0 nm. S **(b)** Same as **(a)**, but for d_{Pt} =4.0 – 12.0 nm.

S6. Estimation of orbital-to-spin conversion ratios in Ta and Pt

Our results show that the orbital MFPs in Ta and Pt are longer than that in W, and are comparable to their respective spin MFPs. This suggests that a portion of the measured orbital signals in Ta and Pt may arise from spin currents generated via spin-orbit conversion of the injected orbital currents, subsequently contributing to the ISHE. To analyze this effect quantitatively, we assume that the short orbital MFP in W, $\lambda_L^{\mathrm{intr}}$≈0.35 nm, represents the intrinsic orbital MFP characteristic of HMs. The spin MFPs (λ_S) in Ta and Pt are obtained by fitting the terahertz emission amplitudes as a function of HM-layer thickness d_{HM} in Ta|Fe and Pt|Fe heterostructures, yielding λ_S=1.34 nm and 2.00 nm, respectively. We further introduce a conversion ratio r, which quantifies the fraction of orbital currents converted into spin currents. The resulting profile along z is modeled by the normalized distribution:

$$f(z) = e^{-\frac{z}{\lambda_L^{\mathrm{intr}}}} + \frac{r\cdot\Gamma}{1-r}\cdot\frac{\lambda_S}{\lambda_S-\lambda_L^{\mathrm{intr}}}\left(e^{-\frac{z}{\lambda_S}} - e^{-\frac{z}{\lambda_L^{\mathrm{intr}}}}\right), \tag{S3}$$

where $\Gamma = |\gamma_{\mathrm{SH}}/\gamma_{\mathrm{OH}}|$. The values of Γ for Ta and Pt are ~0.1 and ~0.4, respectively, according to Ref. 9,10. We use Eq. (S3) to fit the experimentally extracted orbital current density distributions, which follow an exponential decay $e^{-\frac{z}{\lambda_L^{\mathrm{expt}}}}$, with the $\lambda_L^{\mathrm{expt}}$ values listed in Table 1 of the main text. This fitting allows us to extract the orbital-to-spin conversion ratio r for Ta and Pt (Fig. S18). There results, shown in Fig. S18, yield r=81% for Ta and 48% for Pt.

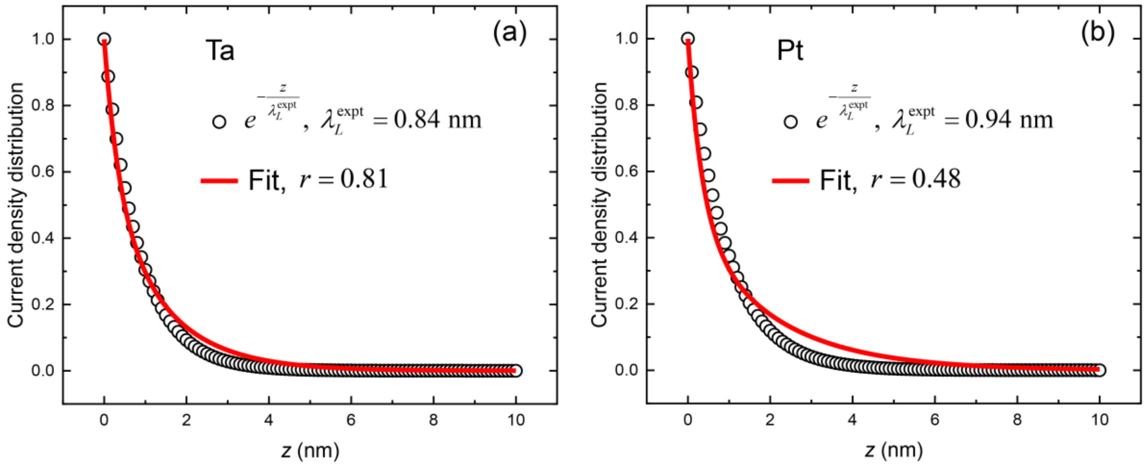

Figure S18. (a) Fitting results to the experimental orbital distribution of Ta $e^{-\frac{z}{\lambda_L^{\text{expt}}}}$.
(b) Same as **(a)**, but for Pt.

Reference

1. Ordal, M. A., Bell, R. J., Alexander, R. W., Newquist, L. A. & Querry, M. R. Optical properties of Al, Fe, Ti, Ta, W, and Mo at submillimeter wavelengths. *Appl. Opt.* **27**, 1203 (1988).
2. Polyanskiy, M. N. Refractiveindex.info database of optical constants. *Sci. Data* **11**, 94 (2024).
3. Tselin, A. *et al.* Exploring the dielectric function of platinum. *Phys. Rev. B* **110**, 195130 (2024).
4. Liu, Y. *et al.* Separation of emission mechanisms in spintronic terahertz emitters. *Phys. Rev. B* **104**, 064419 (2021).
5. Duvillaret, L., Garet, F. & Coutaz, J. L. A reliable method for extraction of material parameters in terahertz time-domain spectroscopy. *IEEE J. Sel. Top. Quantum Electron.* **2**, 739–745 (1996).
6. Gao-Fang, L. *et al.* Properties of Terahertz spectral in aluminium oxide crystal[J]. *J. Infrared Millim. Waves* **40**, 38–43 (2021).
7. Laman, N. & Grischkowsky, D. Terahertz conductivity of thin metal films. *Appl. Phys. Lett.* **93**, 051105 (2008).
8. Walther, M. *et al.* Terahertz conductivity of thin gold films at the metal-insulator percolation transition. *Phys. Rev. B* **76**, 125408 (2007).
9. Kontani, H., Tanaka, T., Hirashima, D. S., Yamada, K. & Inoue, J. Giant orbital hall effect in transition metals: Origin of large spin and anomalous hall effects. *Phys. Rev. Lett.* **102**, 016601 (2009).
10. Salemi, L. & Oppeneer, P. M. First-principles theory of intrinsic spin and orbital Hall and Nernst effects in metallic monoatomic crystals. *Phys. Rev. Mater.* **6**, 095001 (2022).